International Journal of Heat and Mass Transfer 52 (2009) 2824–2833

Contents lists available at ScienceDirect

International Journal of Heat and Mass Transfer

journal homepage: www.elsevier.com/locate/ijhmt

Visualization of heat flow due to natural convection within triangular cavities using Bejan's heatline concept

Tanmay Basak [a], G. Aravind [a], S. Roy [b,*]

[a] Department of Chemical Engineering, Indian Institute of Technology Madras, Chennai 600 036, India
[b] Department of Mathematics, Indian Institute of Technology Madras, Chennai 600 036, India

ARTICLE INFO

Article history:
Received 15 April 2008
Received in revised form 6 October 2008
Available online 11 February 2009

Keywords:
Heatlines
Heatfunction
Inverted triangular cavity
Streamlines
Streamfunctions
Natural convection

ABSTRACT

Natural convection and flow circulation within a cavity has received significant attention in recent times. The wide range of applicability of flow inside a cavity (food processing industries, molten metal industries, etc.) requires thorough understanding for cost efficient processes. This paper is based on comprehensive analysis of heat flow pattern using Bejan's heatline concept. The key parameters for our study are the Prandtl number, Rayleigh number and Nusselt number. The values of Prandtl number (0.015, 0.026, 0.7 and 1000) have been chosen based on wide range of applicability. The Rayleigh number has been varied from 10^2 to 10^5. Interesting results were obtained. For low Rayleigh number, it is found that the heatlines are smooth and perfectly normal to the isotherms indicating the dominance of conduction. But as *Ra* increases, flow slowly becomes convection dominant. It is also observed that multiple secondary circulations are formed for fluids with low *Pr* whereas these features are absent in higher *Pr* fluids. Multiple circulation cells for smaller *Pr* also correspond multiple cells of heatlines which illustrate less thermal transport from hot wall. On the other hand, the dense heatlines at bottom wall display enhanced heat transport for larger *Pr*. Further, local heat transfer (Nu_l,Nu_t) are explained based on heatlines. The comprehensive analysis is concluded with the average Nusselt number plots. A correlation for average heat transfer rate and *Ra* has been developed and the range of Rayleigh number is also found, to depict the conduction dominant heat transfer.

1. Introduction

The relevance of buoyancy induced circulations causing transport of heat and mass is significant in various physical systems. Especially, the applicability of natural convection inside triangular enclosure, in wide range of engineering processes from energy related to geophysical and material processing industry is very well known [1–6]. In particular, convective heat transfer is widely used in material processing industries like food industries, molten salt application (e.g. fuel cell technology), molten metal applications, etc. [7,8]. Various other studies involving sterilization, solidification of food, food separation processes and other natural convection based processes have also been reported by earlier researchers [9–13]. The analysis of flow for such systems is important for a complete understanding of the problem. Numerical modeling may be employed to understand and analyze these systems. The advantage of numerical simulations is that the expensive experimental costs can be reduced.

Numerical and experimental studies on natural convection in triangular cavities have received significant attention due to various applications. Poulikakos and Bejan [14] have carried out extensive analysis on natural convection in an attic space. Holtzman et al. [15] and Del Campo et al. [16] did numerical study of natural convection in triangular enclosures. Later, Kent et al. [17] and Omri et al. [18] carried out numerical study on right-angled and isosceles triangular cavities, respectively. Varol et al. [19] did the study of natural convection in a triangular enclosure with flush mounted heater on the wall. Recently, Sieres et al. [20] carried out analysis of convection within a triangular enclosure for cavities with variable aperture. A few other recent investigations on natural convection within triangular cavities for various applications have been carried out by earlier researchers [21–26]. However, a comprehensive analysis on natural convection flows in complex enclosures is yet to appear in the literature. It is essential to study the heat transfer characteristics in complex geometries to obtain optimal design of the processes for improving the product quality.

Although a number of numerical investigations [17–26] has been carried out in triangular cavities, the detailed analysis of heat flow was poorly understood. The motivation for this work arises from the fact that there is a lack on visualization of heat flow to analyze the optimal thermal mixing and temperature distribution within triangular enclosures. In view of various applications of thermal processes, a comprehensive understanding of heat transfer

* Corresponding author.
E-mail addresses: tanmay@iitm.ac.in (T. Basak), sjroy@iitm.ac.in (S. Roy).

0017-9310/$ - see front matter © 2009 Elsevier Ltd. All rights reserved.
doi:10.1016/j.ijheatmasstransfer.2008.10.034

Nomenclature

g	acceleration due to gravity (m s^{-2})
k	thermal conductivity (W m^{-1} K^{-1})
L	height of the triangular cavity (m)
N	total number of nodes
Nu	Nusselt number
$\overline{Nu}$	average Nusselt number
p	pressure (Pa)
P	dimensionless pressure
Pr	Prandtl number
R	residual of weak form
Ra	Rayleigh number
T	temperature (K)
T_h	temperature of hot inclined wall (K)
T_c	temperature of cold top wall (K)
u	x component of velocity (m s^{-1})
U	x component of dimensionless velocity
v	y component of velocity (m s^{-1})
V	y component of dimensionless velocity
X	dimensionless distance along x-coordinate
x	distance along x-coordinate (m)
Y	dimensionless distance along y-coordinate
y	distance along y-coordinate (m)

Greek symbols

α	thermal diffusivity (m^2 s^{-1})
β	volume expansion coefficient (K^{-1})
γ	penalty parameter
Γ	boundary
θ	dimensionless temperature
ν	kinematic viscosity (m^2 s^{-1})
ρ	density (kg m^{-3})
Φ	basis functions
ψ	dimensionless streamfunction
Π	dimensionless heatfunction

Subscripts

i	residual number
k	node number
l	left wall
r	right wall
t	top wall

and flow circulations within triangular cavities is very much essential for industrial development. Current work attempts to analyze heat transfer, correlations and energy distributions using heatline approach.

The heatline concept was first introduced by Kimura and Bejan [27] and Bejan [28]. Heatline is the best tool to analyze and understand the heat flow in 2D convective transport processes and this concept is similar to streamline which is important to analyze fluid motion. Heatlines represent heatflux lines which represent the trajectory of heat flow and they are normal to the isotherms for conductive heat transfer. It may be noted that heatfunctions are mathematical representations of heatlines and each heatline contour corresponds to constant heatfunction. Various applications using heatlines were studied by Bello-Ochende [29], Costa [30–33], Mukhopadhyay et al. [34,35] and Deng and Tang [36]. Recently, Dalal and Das [37] have used heatline method for the visualization of flow in a complicated cavity. However, a comprehensive analysis on heat flow during natural convection in a triangular cavity with the heatline approach is yet to appear in the literature.

The aim of this paper is to study the circulations and temperature distribution and to analyze the flow of heat due to natural convection in an isosceles right angled inverted triangular enclosure with an aspect ratio of 2:1, involving hot inclined walls and cold top wall. The geometry of this enclosure with boundary conditions is shown in Fig. 1. Numerical results are presented in terms of isotherms, streamlines and heatlines along with the local and average heat transfer rates. Galerkin finite element method with penalty parameter has been used to solve the non-linear coupled partial differential equations of flow and temperature fields. To solve the Poisson equation for streamfunctions and heatfunctions, Galerkin method is also used. It may be noted that Galerkin method has been used to evaluate heatfunction for the first time in this work. The jump discontinuity in Dirichlet type of wall boundary conditions for temperature at the corner points correspond to computational singularities. This problem is tackled by considering the average temperature of the two walls at the corner and keeping the adjacent grid nodes at the respective wall temperature similar to earlier works. We have considered Prandtl number from low to high range (0.015–1000) for fluids of various industrial applications. Typically, $Pr = 0.015$ corresponds to molten metals and $Pr = 988.24$ corresponds to olive oil. Non-orthogonal grid generation is done with iso-parametric mapping as given in Appendix A.

2. Governing equations and solution procedure

2.1. Momentum and energy formulation

The fluid properties are assumed to be constant except the density in the body force term which was determined according to the Boussinesq approximation. This approximation is used in the field of buoyancy driven flows and it is based on the fact that density in the body force term varies linearly with temperature. Under these assumptions, the governing equations for steady two dimensional, laminar, incompressible flows can be written in dimensionless form as:

$$\frac{\partial U}{\partial X} + \frac{\partial V}{\partial Y} = 0, \tag{1}$$

$$U\frac{\partial U}{\partial X} + V\frac{\partial U}{\partial Y} = -\frac{\partial P}{\partial X} + Pr\left(\frac{\partial^2 U}{\partial X^2} + \frac{\partial^2 U}{\partial Y^2}\right), \tag{2}$$

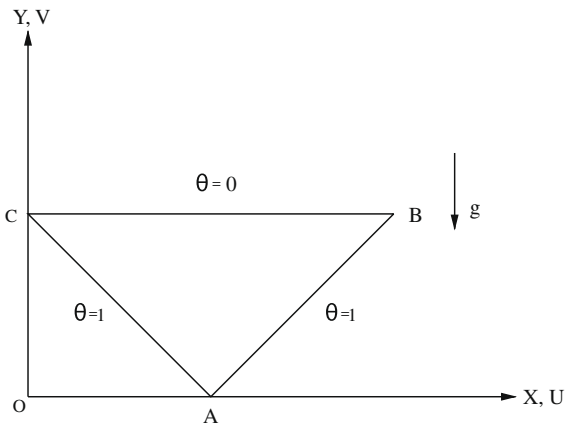

Fig. 1. Schematic diagram of the physical system with the boundary conditions.

$$U\frac{\partial V}{\partial X}+V\frac{\partial V}{\partial Y}=-\frac{\partial P}{\partial Y}+Pr\left(\frac{\partial^2 V}{\partial X^2}+\frac{\partial^2 V}{\partial Y^2}\right)+Ra\,Pr\,\theta, \tag{3}$$

$$U\frac{\partial \theta}{\partial X}+V\frac{\partial \theta}{\partial Y}=\frac{\partial^2 \theta}{\partial X^2}+\frac{\partial^2 \theta}{\partial Y^2}, \tag{4}$$

where

$$X=\frac{x}{L},\quad Y=\frac{y}{L},\quad U=\frac{uL}{\alpha},\quad V=\frac{vL}{\alpha},\quad \theta=\frac{T-T_c}{T_h-T_c}$$
$$P=\frac{pL^2}{\rho\alpha^2},\quad Pr=\frac{v}{\alpha},\quad Ra=\frac{g\beta(T_h-T_c)L^3Pr}{v^2}. \tag{5}$$

In Eq. (5), X and Y are the dimensionless distances along x- and y-coordinate, respectively, L is vertical depth of the cavity, i.e. perpendicular distance of the bottom corner from top horizontal wall, U and V are the corresponding velocity components along the coordinate axes, P denotes the dimensionless pressure whereas Pr and Ra denote Prandtl number and Rayleigh numbers, respectively. No slip conditions are assumed at all the walls and the boundary conditions for the velocity components are

$$\begin{aligned} &U(X,1)=V(X,1)=0 \quad \text{on BC},\\ &U(X,Y)=V(X,Y)=0 \quad \text{on AC},\\ &U(X,Y)=V(X,Y)=0 \quad \text{on AB}. \end{aligned} \tag{6}$$

The boundary conditions for temperature are

$$\begin{aligned} &\theta(X,1)=0 \quad \text{on BC},\\ &\theta(X,Y)=1 \quad \text{on AC},\\ &\theta(X,Y)=1 \quad \text{on AB}. \end{aligned} \tag{7}$$

The continuity equation (1) is used as a constraint due to mass conservation and this constraint can be used to obtain the pressure distribution. The momentum and energy balance equations [Eqs. (2)–(4)] are solved using Galerkin finite element method. In order to solve Eqs. (2) and (3), penalty finite element method has been employed to eliminate the pressure P with a penalty parameter γ and the incompressibility criteria given by Eq. (1) via following relationship:

$$P=-\gamma\left(\frac{\partial U}{\partial X}+\frac{\partial V}{\partial Y}\right). \tag{8}$$

Typically $\gamma=10^7$ yields consistent solutions. Applying Eq. (8), the momentum balance equations [Eqs. (2) and (3)], are reduced to

$$U\frac{\partial U}{\partial X}+V\frac{\partial U}{\partial Y}=\gamma\frac{\partial}{\partial X}\left(\frac{\partial U}{\partial X}+\frac{\partial V}{\partial Y}\right)+Pr\left(\frac{\partial^2 U}{\partial X^2}+\frac{\partial^2 U}{\partial Y^2}\right), \tag{9}$$

and

$$U\frac{\partial V}{\partial X}+V\frac{\partial V}{\partial Y}=\gamma\frac{\partial}{\partial Y}\left(\frac{\partial U}{\partial X}+\frac{\partial V}{\partial Y}\right)+Pr\left(\frac{\partial^2 V}{\partial X^2}+\frac{\partial^2 V}{\partial Y^2}\right)+RaPr\theta. \tag{10}$$

The system of equations [Eqs. (9), (10) and (4)] with appropriate boundary conditions are solved using Galerkin finite element method as discussed in earlier references [26,38,39].

2.2. Streamfunction and heatfunction

The fluid motion is displayed using the streamfunction, ψ, obtained from velocity components U and V. The relationships between streamfunction, ψ and velocity components for two-dimensional flows are

$$U=\frac{\partial \psi}{\partial Y}\quad \text{and}\quad V=-\frac{\partial \psi}{\partial X}, \tag{11}$$

which yield a single equation

$$\frac{\partial^2 \psi}{\partial X^2}+\frac{\partial^2 \psi}{\partial Y^2}=\frac{\partial U}{\partial Y}-\frac{\partial V}{\partial X}. \tag{12}$$

The sign convention is that, positive sign of ψ denotes anti-clockwise circulation and clockwise circulation is represented by negative sign of ψ. The no-slip condition is valid at all boundaries as there is no cross flow, hence $\psi=0$ is used for boundaries. Streamfunctions corresponding to fluid velocities are obtained using finite element method as discussed earlier [26,38,39].

The heat flow within the enclosure is displayed using the heatfunction (Π) obtained from conductive heat fluxes $\left(-\frac{\partial\theta}{\partial X},-\frac{\partial\theta}{\partial Y}\right)$ as well as convective heat fluxes ($U\theta$,$V\theta$). The heatfunction satisfies the steady energy balance equation [Eq. (4)] [27] such that

$$\begin{aligned} &\frac{\partial \Pi}{\partial Y}=U\theta-\frac{\partial \theta}{\partial X},\\ &-\frac{\partial \Pi}{\partial X}=V\theta-\frac{\partial \theta}{\partial Y}, \end{aligned} \tag{13}$$

which yield a single equation

$$\frac{\partial^2 \Pi}{\partial X^2}+\frac{\partial^2 \Pi}{\partial Y^2}=\frac{\partial}{\partial Y}(U\theta)-\frac{\partial}{\partial X}(V\theta). \tag{14}$$

The sign convention for heatfunction is as follows. The positive sign of Π denotes anti-clockwise heat flow and clockwise heat flow is represented by negative sign of Π. Heatfunctions are obtained via finite element method similar to the procedure for evaluation of streamfunctions.

In order to obtain an unique solution of Eq. (14), following boundary conditions are implemented. Neumann boundary conditions for Π are obtained due to isothermal (hot or cold) wall based on Eq. (13) and for isothermal (hot or cold) wall

$$\mathbf{n}\cdot\nabla\Pi=0. \tag{15}$$

The following are the Dirichlet boundary conditions:

$$\Pi=\sqrt{2}\overline{Nu_l}\quad \text{at } X=0,\ Y=1, \tag{16}$$

$$\Pi=0\quad \text{at } X=1,\ Y=0, \tag{17}$$

and

$$\Pi=-\sqrt{2}\overline{Nu_r}\quad \text{at } X=2,\ Y=1. \tag{18}$$

It may be noted that, $\overline{Nu_l}$ and $\overline{Nu_r}$ are average Nusselt numbers at the left and right walls, respectively. The details on evaluation of Nusselt numbers are discussed next.

The heat transfer coefficient in terms of local Nusselt number (Nu) is defined by

$$Nu=-\frac{\partial \theta}{\partial n}. \tag{19}$$

Here n denotes the normal direction of the plane. The local Nusselt numbers at top wall(Nu_t), left wall(Nu_l) and right wall(Nu_r) are defined as

$$Nu_t=-\sum_{i=1}^{9}\theta_i\frac{\partial \Phi_i}{\partial Y}, \tag{20}$$

$$Nu_l=\sum_{i=1}^{9}\theta_i\left(\frac{1}{\sqrt{2}}\frac{\partial \Phi_i}{\partial X}+\frac{1}{\sqrt{2}}\frac{\partial \Phi_i}{\partial Y}\right), \tag{21}$$

and

$$Nu_r=\sum_{i=1}^{9}\theta_i\left(-\frac{1}{\sqrt{2}}\frac{\partial \Phi_i}{\partial X}+\frac{1}{\sqrt{2}}\frac{\partial \Phi_i}{\partial Y}\right). \tag{22}$$

The average Nusselt numbers at the top and side walls are

$$\overline{Nu_t}=\frac{\int_0^2 Nu_t\,dX}{\int_0^2 dX}=\frac{1}{2}\int_0^2 Nu_t\,dX \tag{23}$$

and

$$\overline{Nu_l} = \overline{Nu_r} = \frac{1}{\sqrt{2}} \int_0^{\sqrt{2}} Nu_l \, dS. \quad (24)$$

Here dS denotes the elemental length along inclined sides of the triangular cavity.

3. Results and discussion

3.1. Numerical tests

The computational domain in ξ–η-coordinates (see Appendix A) consists of 20×20 bi-quadratic elements which correspond to 41×41 grid points. Note that, the computational grid in the triangular domain is generated via mapping the triangular domain into square domain in ξ–η-coordinate system as shown in Fig. 2 and the procedure is outlined in Appendix A. The bi-quadratic elements with lesser number of nodes smoothly capture the non-linear variations of the field variables which are in contrast with finite difference/finite volume solutions available in the literature [22].

In the current investigation, Gaussian quadrature based finite element method provides the smooth solutions at the interior domain including the corner regions as evaluation of residuals depends on the interior Gauss points and thus the effect of corner nodes are less profound in the final solution. In general, the Nusselt numbers for finite difference/finite volume based methods are calculated at any surface using some interpolation functions which are now avoided in the current work. The present finite element method based approach offers special advantage on evaluation of local Nusselt number at the left, right and top walls as the element basis functions have been used here to evaluate the heatflux [39]. Our simulation studies on isotherm and streamline have also been compared with earlier studies [22] and the results are in well agreement. In this study, Prandtl number is varied from 0.015 to 1000 covering wide range of applications. Also, Rayleigh number effects with $Ra = 10^2$–10^5 have been studied. Variation of Nusselt number with distance and Rayleigh number, and also, variation of average Nusselt number vs. Rayleigh number have been shown to illustrate heat transfer rates. Detailed explanation is given in various succeeding sections.

3.2. Isotherms, streamlines and heatlines

Due to the temperature gradient imposed by hot side walls and cold top wall and the buoyancy force, hot (lighter) fluid tends to move near the top wall and cold (heavier) fluid tends to move towards bottom. Hot fluid along the inclined walls moving towards the top wall and cold fluid from the center of top wall tending to move towards the bottom wall lead to two oppositely circulating rolls in the system. It is observed that the symmetric flow and temperature patterns occur for $Ra = 10^2$–10^5 with all representative Pr values based on symmetric thermal boundary conditions at inclined side walls. Based on the physical systems, the left half of the axis of symmetry gives clockwise circulation pattern. The symmetric solutions for the parameter ranges have been obtained based on solutions of governing equations within the entire domain. The non-symmetric solutions even with some specific symmetric boundary conditions in rectangular domains were found for some other parameter ranges [40] and the investigations on non-symmetric solutions for the triangular domains are the subject of future research.

Firstly, flow and thermal dynamics for $Pr = 0.015$ are reported for various Rayleigh numbers (see Figs. 3–5). At low Rayleigh number ($Ra = 10^2$), the isotherms are smooth and monotonic and the magnitude of streamlines are quite small (see Fig. 3a and b). This shows that at small Ra, heat transfer is mostly conduction dominant. The isotherms span the entire enclosure and they are symmetric with respect to the vertical center line.

The heatlines are constructed based on heat flux boundary conditions and the corner edges of the top wall are maintained at average Nusselt number ($\Pi = \overline{Nu_l}$) as the bottom edge is maintained at $\Pi = 0$. Therefore, the large values of Π at the edges of the top wall

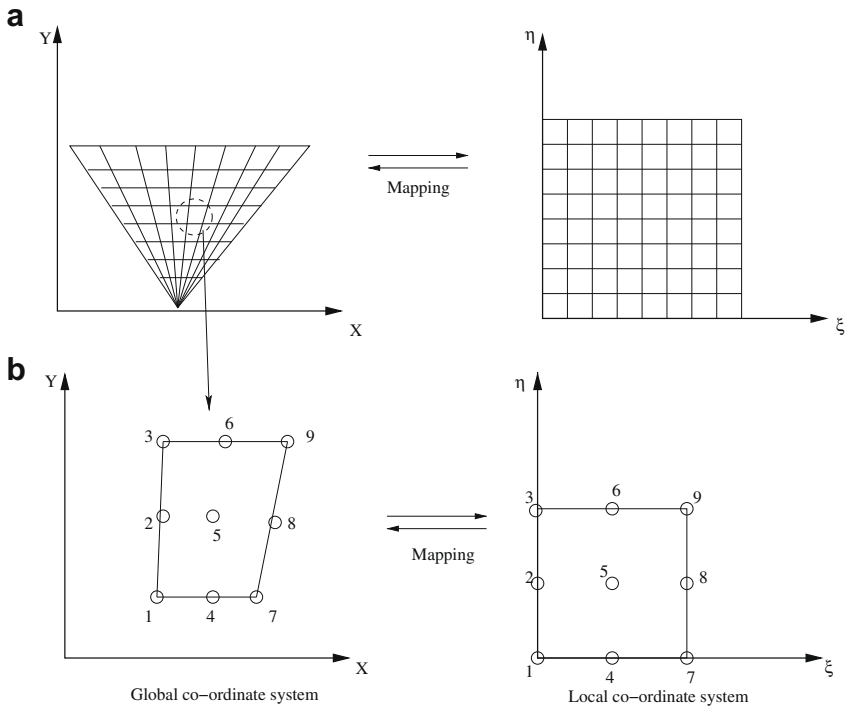

Fig. 2. (a) The mapping of triangular domain to a square domain in ξ–η-coordinate system and (b) the mapping of an individual element to a single element in ξ–η-coordinate system.

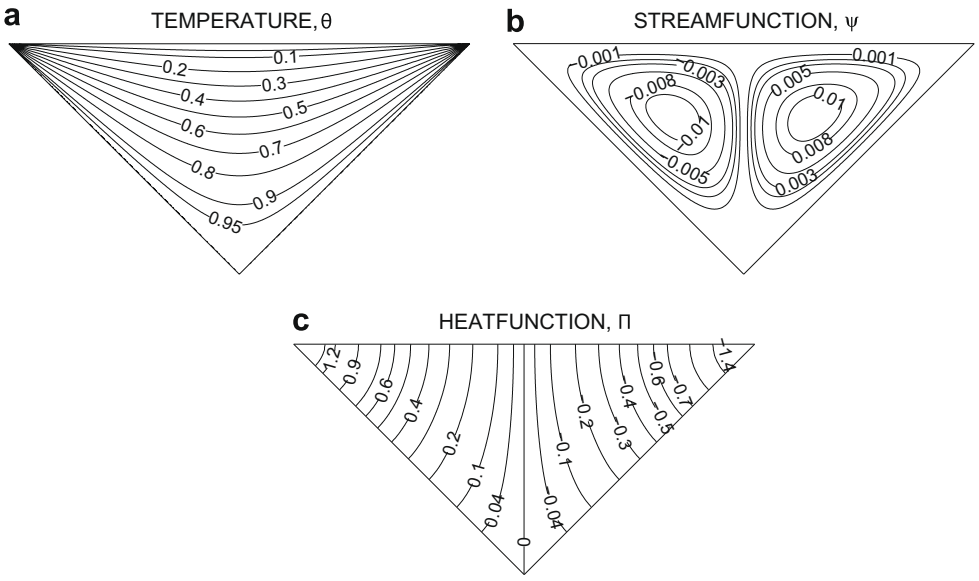

Fig. 3. (a) Temperature (θ), (b) streamfunction (ψ), and (c) heatfunction (Π) contours with $Pr = 0.015$ and $Ra = 10^2$. Clockwise and anti-clockwise flows are shown via negative and positive signs of streamfunctions and heatfunctions, respectively.

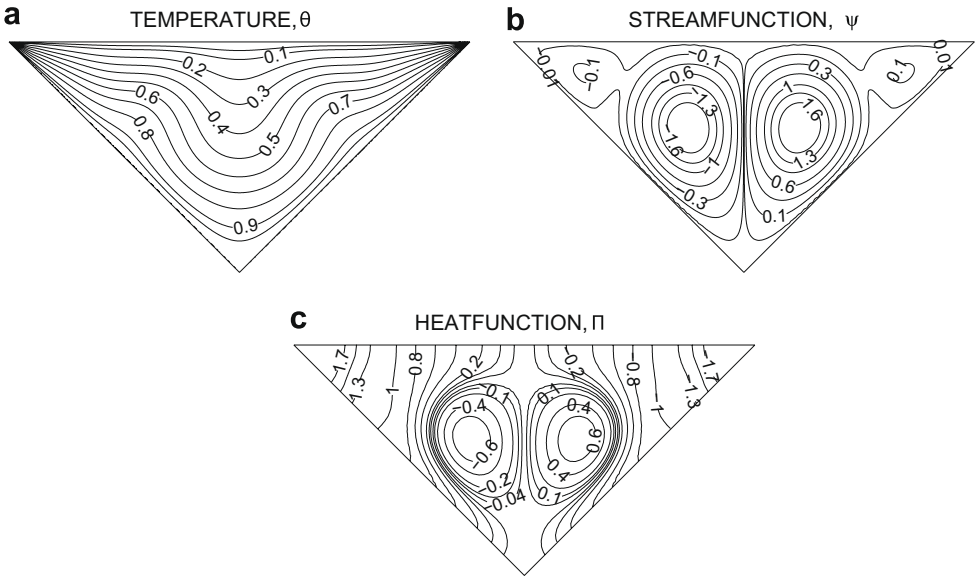

Fig. 4. (a) Temperature (θ), (b) streamfunction (ψ), and (c) heatfunction (Π) contours with $Pr = 0.015$ and $Ra = 10^4$. Clockwise and anti-clockwise flows are shown via negative and positive signs of streamfunctions and heatfunctions, respectively.

are mainly due to the cold wall being directly in contact with hot inclined walls. The basis of the sign convention is that heat flows from hot to cold wall and the positive heatfunction corresponds to anti clockwise heat flow. Fig. 3c illustrates that the heat flow occurs mainly due to the conduction as the heatlines are nearly perpendicular to the isotherm lines as well as the walls. An important point to note is that the heatlines with greater strength are clustered around the top portion of the inclined wall and as we move down along the inclined wall, the strength of heatline goes to as low as 0.04. This means that major amount of heat flux or transport occurs near the cold wall. Thus, relatively less heat flow occurs from the bottom edge of the enclosure. It is also illustrated that the top cold wall receives most of the heat from the upper half of hot inclined walls during conduction dominant heat transfer.

As Rayleigh number is increased to 10^4 (Fig. 4a–c), isotherms tend to deform but they are symmetric to the vertical central line and the deformation is due to the presence of significant convection in the system (Fig. 4a). It is also observed that the intensity of buoyancy driven circulations inside the cavity increases as seen from greater strength of streamfunctions. Intensity of circulations are greater near the center and least at the wall due to no slip boundary conditions. Secondary circulations are also developed near the intersection of inclined walls with the cold top wall. The heatlines illustrate that, convection dominant effect plays critical role on larger heat to flow from the bottom portion of inclined walls to the top wall (Fig. 4c). It is observed that the heatlines are less dense near the top corner points where heat transport is conduction dominant as the intensity of fluid circulation is less as seen from streamfunctions. Although the infinite heat transfer occurs at the top corner points, the heatlines are less dense near those points due to absence of convection. It is interesting to observe that the heatlines are quite dense near the bottom portions

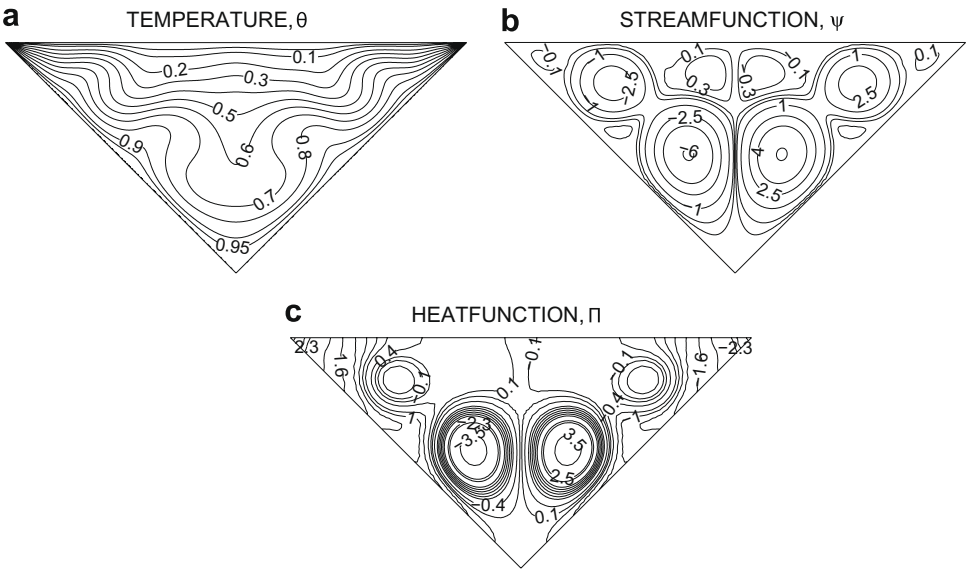

Fig. 5. (a) Temperature (θ), (b) streamfunction (ψ), and (c) heatfunction (Π) contours with $Pr = 0.015$ and $Ra = 10^5$. Clockwise and anti-clockwise flows are shown via negative and positive signs of streamfunctions and heatfunctions, respectively.

of inclined walls and that specifies more heat transfer from the regime near the bottom corner to the top cooled wall. Also, it is seen that the shape of heatlines near the core is identical to that of streamlines signifying the convection dominant heat flow due to large intensity of circulations (large values of streamfunctions). Therefore, the temperature gradients as seen from Fig. 4a are less near the center of each half due to large heat distribution resulting from convective heat transfer.

As Rayleigh number is increased to 10^5 (Fig. 5a–c), multiple and stronger circulations appear and those result in more deformations in the isotherms. It may be noted that the magnitude of streamfunctions are larger for $Ra = 10^5$ signifying the larger intensity of circulations. Multiple circulations greatly influence the heatline patterns and heat distributions as seen in Fig. 5c. Similar to previous case (Fig. 4), the top portions of the inclined hot walls do not distribute much heat to the cold wall. Note that, the intensity of fluid circulations is found to be much stronger near the bottom corner for $Ra = 10^5$. This strong convection cell distributes heat from the bottom portion of hot walls and thus enhanced convective heat transfer occurs as seen from dense heatline contours. Therefore, the temperature gradient is less due to enhanced thermal mixing near bottom potion of the central regime. In contrast, the heatlines were found to be less dense near the horizontal wall where the heat transport is mainly due to conduction.

Next, the effect of change in Prandtl number has been investigated. Fig. 6 illustrates distribution for $Pr = 0.026$ and $Ra = 10^5$. As expected the qualitative trends in flow and thermal characteristics are identical to those in Fig. 5a–c. However, we do see that the number of multiple circulations as illustrated by the streamlines has slightly been decreased especially towards the corners of the top wall. The heatlines show identical quantitatively features for $Pr = 0.015$ and $Pr = 0.026$ (Figs. 5c and 6c). The interesting comparison may be illustrated as Prandtl Number is increased to 0.7 (Fig. 7c). Streamlines illustrate that for $Pr = 0.7$, all the multiple circulations that were observed at $Pr \leqslant 0.026$, have been totally absent (Fig. 7b). The streamlines are now elliptical towards the center and smooth triangular

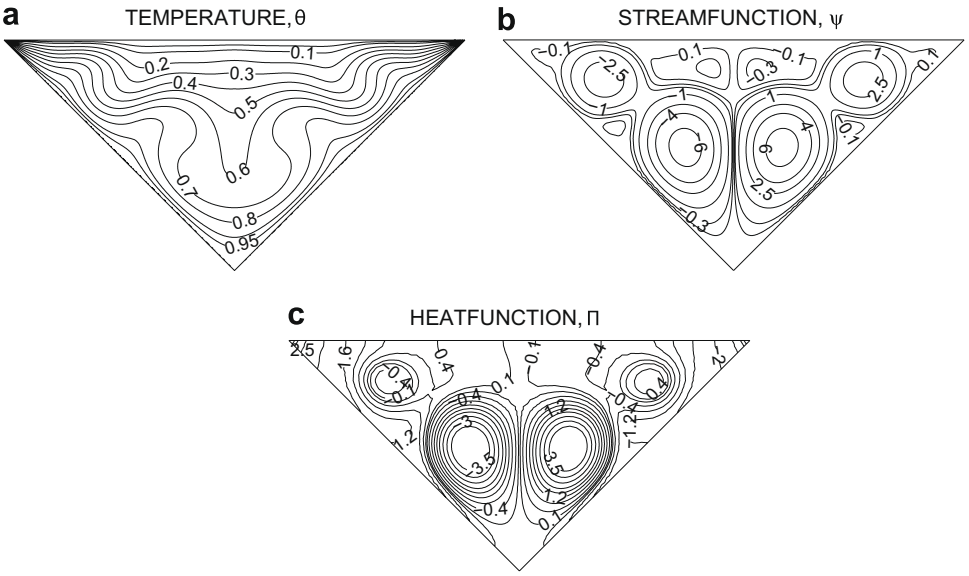

Fig. 6. (a) Temperature (θ), (b) streamfunction (ψ), and (c) heatfunction (Π) contours with $Pr = 0.026$ and $Ra = 10^5$. Clockwise and anti-clockwise flows are shown via negative and positive signs of streamfunctions and heatfunctions, respectively.

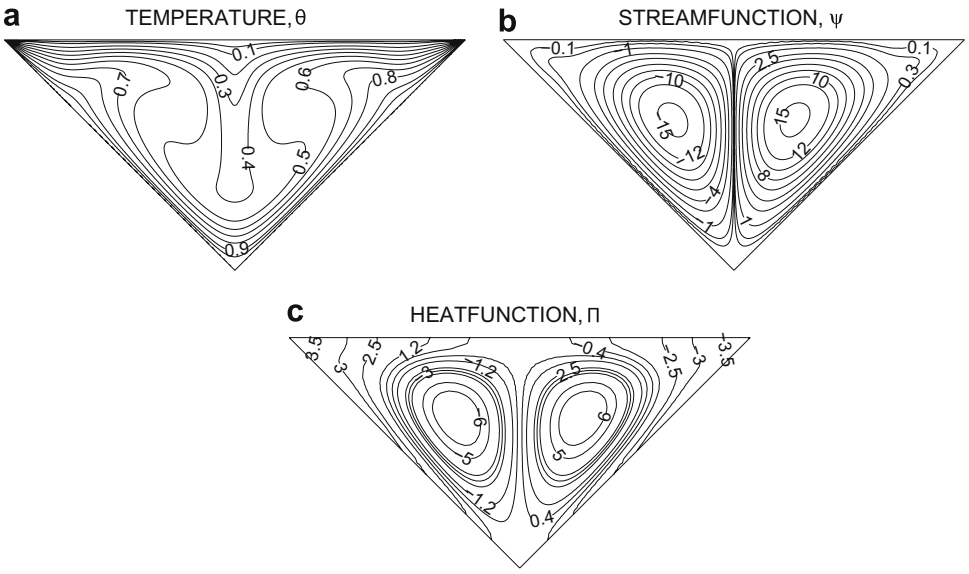

Fig. 7. (a) Temperature (θ), (b) streamfunction (ψ), and (c) heatfunction (Π) contours with $Pr = 0.7$ and $Ra = 10^5$. Clockwise and anti-clockwise flows are shown via negative and positive signs of streamfunctions and heatfunctions, respectively.

curves near the walls. The intensity of the flow has been tremendously increased. The strength of the streamfunction has been increased to almost double near the center regime. The heatlines are similar to streamlines at the core signifying convective heat flow and a large amount of heat flow occurs from the bottom portion of inclined wall as seen from dense heatlines.

Fig. 8a–c illustrates the profiles for large Prandtl number ($Pr = 1000$) with $Ra = 10^5$. It is noteworthy to mention that Figs. 7 and 8 have almost the similar trend for isotherms, streamlines and heatlines. The streamlines become smooth elliptical towards the corner points of the top wall. All the multiple circulations that were seen in previous cases (Figs. 5b and 6b) have been completely disappeared into a single circulation with a central core. The strength of streamfunction at the central regime is larger compared to the previous cases. Identical trend in heatlines is observed based on Figs. 5 and 6c and Figs. 7 and 8c. The absence of multiple heat circulations in the system is observed and a very intense heat flow occurs across the inclined walls represented by dense heatline for $Pr = 0.7, 1000$. It is interesting to observe that heat transport in a large regime at the core is due to convection. The large regime of convection is due to the large amount of heat transport from the inclined walls associated with large intensity of circulations (Figs. 7c and 8c). The convective heat transport has been suppressed for lower Pr due to the presence of multiple circulations.

3.3. Heat transfer rate: Nusselt numbers

Fig. 9a shows the variation of heat transfer rate (Nu_r, Nu_l) along the inclined wall. A wavy distribution pattern for the heat transfer rate is observed for $Pr = 0.015$ and $Ra = 10^5$. The heat transfer rate is quite small till the distance being 0.2, as this region is near the intersection of hot walls, resulting in low heat transfer between the fluid. Thereafter heat transfer rate steadily increases until the distance being 0.4. The same pattern is observed again after distance 0.6 until up to 0.8. The wavy pattern occurs due to the multiple circulations cells with low Prandtl numbers for $Ra = 10^5$ (see Figs. 5b

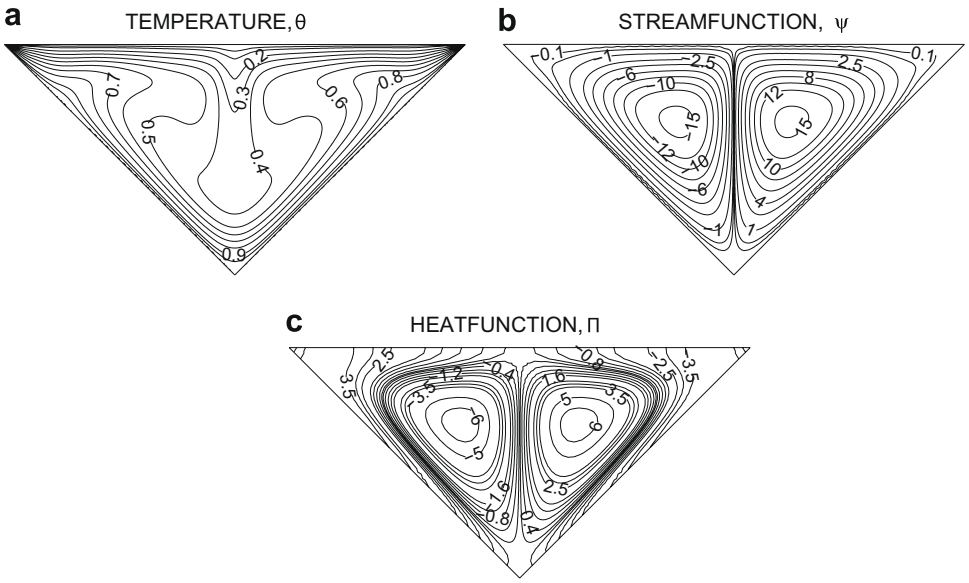

Fig. 8. (a) Temperature (θ), (b) streamfunction (ψ), and (c) heatfunction (Π) contours with $Pr = 1000$ and $Ra = 10^5$. Clockwise and anti-clockwise flows are shown via negative and positive signs of streamfunctions and heatfunctions, respectively.

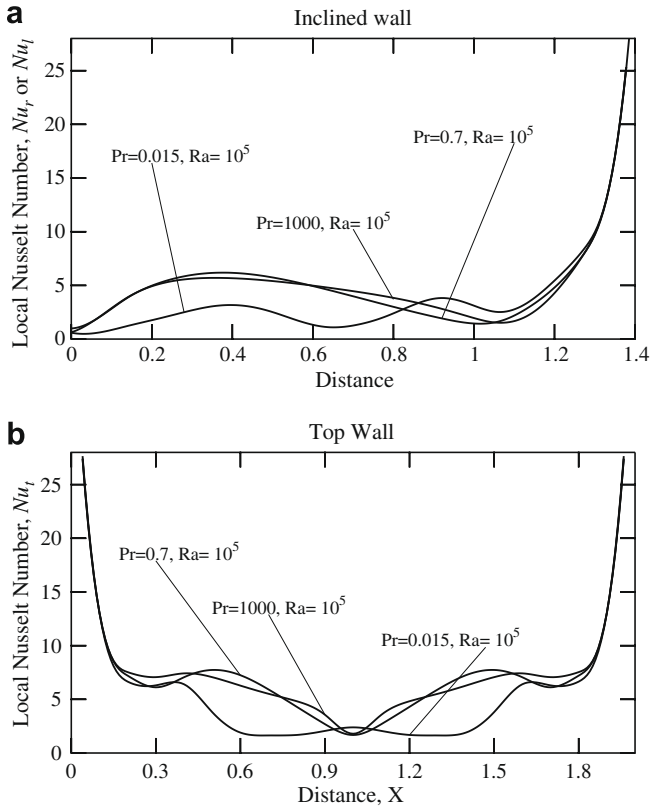

Fig. 9. Variation of local Nusselt number with distance for various Pr (0.015, 0.7, 1000) with $Ra = 10^5$ at (a) inclined wall and (b) top wall.

and 6b). Each circulation cell is characterized by an intense central core region and a less intensified outer region. As a result, the heat transfer starts to decrease at the zone of intersection of two circulation cells. The heatlines are also less dense at the zone between two circulation cells (Fig. 5c). In contrast, the absence of wavy pattern for Nusselt number with higher Prandtl numbers ($Pr = 0.7 - 1000$) is due to absence of multiple circulations. A local maxima of Nu_l or Nu_r occurs at the distance being 0.3 for $Pr = 0.7$ and 1000 and this local maxima is attributed to the dense heatlines as seen in Figs. 7c and 8c. After distance being 1, heat transfer rate increases rapidly and at the edge, the rate is infinite, i.e. at the point of intersection of cold and hot walls for all ranges of Pr. The heat transport near the top corner regimes is predominantly by conduction and thereafter there is a sharp fall of Nu_l or Nu_r from the top corner along the inclined wall. The sharp decrease of Nu_l or Nu_r is also attributed to the less dense heatlines as seen in Figs. 5c, 6c, 7c and 8c.

Fig. 9b shows the variation of Nusselt number (Nu_t) with the distance along the top wall. It may be noted that at $X = 0$ and $X = 2$ the heat transfer rate is infinite at all ranges of Pr. This is expected at these points, as the hot wall intersects the cold wall exhibiting maximum heat transfer. The heat transfer rate sharply falls when distance is further increased from $X = 0$ till $X = 0.3$ and heat transfer rate decreases thereafter till $X = 0.6$ especially for $Pr = 0.015$. This is due to the multiple circulation cells for $Pr = 0.015$ (see Fig. 5b). In addition, the less heat transfer rate is due to highly dispersed heatlines, as seen in Fig. 5c. The heat transfer rate remains almost constant and low till $X = 1.4$ for $Pr = 0.015$. It is observed that, the heatlines concentrate within $X \leqslant 0.3$ and heatlines are well dispersed within $0.6 \leqslant X \leqslant 1.4$. The qualitative trend is nearly the same for $Pr = 0.7, 1000$ with $Ra = 10^5$. It is important to note that Nu_t is larger except at the central regime for higher Pr due to dense heatlines with enhanced circulation cells (Figs. 7c and 8c) whereas, the heat transfer rate (Nu_t) for $Pr = 0.015$ is

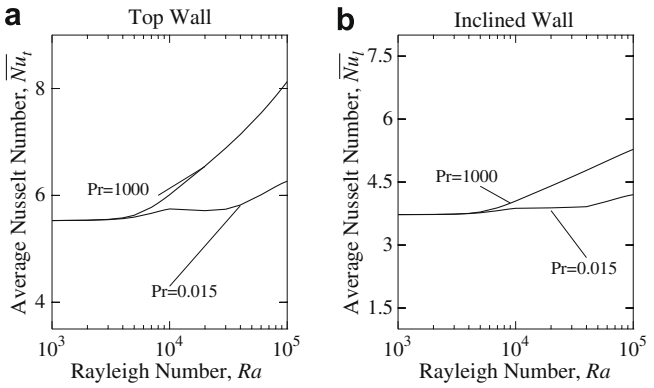

Fig. 10. Variation of average Nusselt number with Rayleigh number for (a) top wall and (b) inclined wall for $Pr = 0.015$ and 1000.

lowest at the center attributed by the less dense heatlines (Figs. 7c and 8c).

Fig. 10a and b shows the distributions of the average Nusselt number of top and inclined walls, respectively, vs. the logarithmic Rayleigh number. The average Nusselt number is obtained via Simpson's one third rule [see Eqs. (23) and (24)]. General observation is that the average Nusselt number increases with Rayleigh numbers. Fig. 10a illustrates that the average Nusselt number remains almost constant till $Ra = 4 \times 10^3$ for $Pr = 1000$. Thereafter the average Nusselt number for $Pr = 1000$ increases rapidly to reach a very high value at $Ra = 10^5$ whereas for $Pr = 0.015$, the average Nusselt number does increase but rate of the increase is very low. The smaller variation for Nu_t is due to secondary and multiple circulations and heat transfer in $Pr = 0.015$ (see Fig. 5c) compared to single symmetric highly intense circulation in $Pr = 1000$ (see Fig. 8c). Similar pattern is observed in Fig. 10b for the inclined walls. Based on energy balance, the average Nusselt number of top wall is $\sqrt{2}$ times that of the inclined wall. This result is well matched in all our cases verifying the energy conservation within the system. A correlation has been developed for a generalized relationship between Nu_t or Nu_l and Ra in a convection dominated regime. A correlation for Nu_t or Nu_l and Ra was observed for $Pr = 0.7$–1000, however, correlation could not be obtained for $Pr = 0.015$ as the overall heat transfer rate is small and conduction dominant regime is observed at higher Ra. The limit of Ra is observed as 4×10^3 for $Pr = 1000$ and convection is found to be significant for $Ra \geqslant 4 \times 10^3$ and the following correlation is obtained:

$$\overline{Nu_t} = \sqrt{2}\overline{Nu_l} = 1.8332 Ra^{0.1288}, \quad Pr = 1000, \ 4 \times 10^3 \leqslant Ra \leqslant 10^5. \tag{25}$$

4. Conclusion

The objective of this paper is to understand a physical as well as computational insight due to heat flow for natural convection within a complex enclosure. The system considered here is an inverted triangular cavity which has wide range of applicability in industries as discussed earlier. The key controlling parameters for our analysis are Rayleigh number and Prandtl number which govern the overall heat transfer rate, i.e. Nusselt number. The motivation is to understand the effect of each of these parameters on the heat flow process. In addition, the values of Prandtl numbers (0.015, 0.7, 1000) have been chosen such that the system depicts wide range of commonly used applications. The visualization of heat flow inside any cavity is incomplete unless we know about the heat flow and hence we have introduced the heatlines concept in the triangular cavity, which enables us to understand the heat flow trajectory. During conduction dominant heat transfer, it is observed that the isotherms, stream-

lines and heatlines are found to be monotonic and smooth curves. Also, the heatlines will be perfectly normal to the isotherm during conduction dominant heat transfer. However, as *Ra* increases to 10^4, convection is initiated, and the flow patterns get distorted with initiation of secondary circulation cells. The strong dominance of convection in heat transfer is clearly illustrated via large magnitudes of streamfunctions and heatfunctions when *Ra* is increased to 10^5. Heat transport is mainly due to convection in multiple circulation zones and thus multiple cells in heatline contours are also observed for *Pr* = 0.015 and *Pr* = 0.026. It is interesting to observe that multiple circulations are suppressed for $Pr \geqslant 0.7$ and dense heatlines are observed near the bottom portion of inclined walls. This implies that a large amount of heat is transferred from the bottom portion of the inclined walls. Thus, isotherms are compressed along that regime and uniform higher temperature is observed at the center of the bottom of cavity due to enhanced thermal mixing based on dense heatlines.

Overall analysis of heat transfer is carried out via local and average Nusselt numbers along the inclined and top walls. It is observed that the Nusselt number is quite large at the intersection of inclined and top walls due to infinite heat transfer rate. It is observed that multiple circulations cells results in a wavy pattern of Nusselt number for low Prandtl numbers indicating fluctuating magnitudes of heat transfer rates at various locations along the inclined and top wall. The wavy pattern in spatial distribution of Nusselt number gradually disappears as *Pr* increases. The comprehensive analysis of heat transfer is further supplemented with average Nusselt numbers for the inclined and top wall. Correlation has been developed for *Pr* = 1000 to illustrate convective heat transfer rate and the range of *Ra* is also found to illustrate the conduction dominant zone.

Acknowledgments

The authors would like to thank anonymous reviewers for critical comments and suggestions which improved the quality of the manuscript.

Appendix A

The name iso-parametric derives from the fact that the same parametric function describing the geometry may be used for interpolating spatial variable within an element [38]. Fig. 2 shows the transformation between (x,y) and (ξ,η) coordinates:

$$X = \sum_{k=1}^{9} \Phi_k(\xi,\eta) x_k,$$
$$Y = \sum_{k=1}^{9} \Phi_k(\xi,\eta) y_k.$$

Here (x_k, y_k) are the *X*-, *Y*-coordinates of the *k* nodal points as seen in Fig. 2 and $\Phi_k(\xi,\eta)$ is the basis function. The nine basis functions are:

$$\Phi_1 = (1-3\xi+2\xi^2)(1-3\eta+2\eta^2),$$
$$\Phi_2 = (1-3\xi+2\xi^2)(4\eta-4\eta^2),$$
$$\Phi_3 = (1-3\xi+2\xi^2)(-\eta+2\eta^2),$$
$$\Phi_4 = (4\xi-4\xi^2)(1-3\eta+2\eta^2),$$
$$\Phi_5 = (4\xi-4\xi^2)(4\eta-4\eta^2),$$
$$\Phi_6 = (4\xi-4\xi^2)(-\eta+2\eta^2),$$
$$\Phi_7 = (-\xi+2\xi^2)(1-3\eta+2\eta^2),$$
$$\Phi_8 = (-\xi+2\xi^2)(4\eta-4\eta^2),$$
$$\Phi_9 = (-\xi+2\xi^2)(-\eta+2\eta^2).$$

The above basis functions are used for mapping the triangular domain or elements within the triangle into square domain and the evaluation of integrals of residuals.

References

[1] K.A. Joudi, I.A. Hussein, A.A. Farhan, Computational model for a prism shaped storage solar collector with a right triangular cross section, Energy Conserv. Manage. 45 (2004) 391–409.
[2] C. Lei, J.C. Patterson, Natural convection in a reservoir sidearm subject to solar radiation: experimental observations, Exp. Fluids 32 (2002) 590–599.
[3] E. Boridy, Potential flow past an open spherical cavity, J. Appl. Phys. 67 (11) (1990) 6687–6693.
[4] A. Campo, E.H. Ridouane, Enhancement of natural convection transport in slender right-angled triangular cavities by way of molding the upper insulated wall, J. Enhanced Heat Transfer 12 (4) (2005) 327–341.
[5] A. Omri, J. Ofri, S. Ben Nasrallah, Natural convection effects in solar stills, Int. J. Heat Mass Transfer 183 (1–3) (2005) 173–178.
[6] T.N. Phillips, Natural convection in an enclosed cavity, J. Comput. Phys. 54 (1984) 365–381.
[7] R.J. Park, S.B. Kim, H.D. Kim, S.M. Choi, Natural convection heat transfer with crust formation in the molten metal pool, Nucl. Technol. 127 (1999) 66–80.
[8] B. Mishra, D.L. Olson, Molten salt applications in materials processing, J. Phys. Chem. Solids 66 (2005) 396–401.
[9] S.G. Akterian, K.A. Fikiin, Numerical simulation of unsteady heat conduction in arbitrary shaped canned foods during sterilization processes, J. Food Eng. 21 (1994) 343–354.
[10] A.L. Bol'shov, P.S. Kondratenko, V.F. Strizhov, Natural convection in heat-generating fluids, Phys.-Usp. 44 (2001) 999–1016.
[11] M. Farid, A.G.A. Abdul, A new computational technique for the estimation of sterilization time in canned food, Chem. Eng. Process. 43 (2004) 523–531.
[12] C. Kai, C. Xi, Effects of natural convection on the characteristics of long laminar argon plasma jets issuing upwards or downwards into ambient air, a numerical study, J. Phys. D 37 (2004) 2385–2391.
[13] C.J. Chang, R.A. Brown, Natural convection in steady solidification: finite element analysis of a two-phase Rayleigh–Benard problem, J. Comput. Phys. 53 (1984) 1–27.
[14] D. Poulikakos, A. Bejan, The fluid dynamics of an attic space, J. Fluid Mech. 131 (1983) 251–269.
[15] G.A. Holtzman, R.W. Hill, K.S. Ball, Laminar natural convection in isosceles triangular enclosures heated from below and symmetrically cooled from above, J. Heat Transfer Trans. ASME 122 (2000) 485–491.
[16] E.M. Del Campo, M. Sen, E. Ramos, Analysis of laminar natural convection in a triangular enclosure, Int. J. Heat Mass Transfer 13 (1988) 353–372.
[17] E.F. Kent, E. Asmaz, S. Ozerbay, Laminar natural convection in right triangular enclosures, Heat and Mass Transfer 44 (2) (2007) 187–200.
[18] A. Omri, M. Najjari, S. Ben Nasrallah, Numerical analysis of natural buoyancy-induced regimes in isosceles triangular cavities, Numer. Heat Transfer A 52 (7) (2007) 327–341.
[19] Y. Varol, A. Koca, H.F. Oztop, Natural convection in a triangle enclosure with flush mounted heater on the wall, Int. Commun. Heat Mass Transfer 33 (8) (2006) 951–958.
[20] J. Sieres, A. Campo, E.H. Ridouane, Effect of surface radiation on buoyant convection in vertical triangular cavities with variable aperture angles, Int. J. Heat Mass Transfer 50 (25–26) (2007) 5139–5149.
[21] H. Asan, L. Namli, Numerical simulation of buoyant flow in a roof of triangular cross section under winter day boundary conditions, Energy Build. 33 (2001) 753–757.
[22] H. Asan, L. Namli, Laminar natural convection in a pitched roof of a triangular cross section: summer day boundary conditions, Energy Build. 33 (2000) 69–73.
[23] I. Hajri, A. Omri, S. Ben Nasrallah, A numerical model for the simulation of double-diffusive natural convection in a triangular cavity using equal order and control volume based on the finite element method, Desalination 206 (1–3) (2007) 579–588.
[24] Y. Varol, H.F. Oztop, A. Varol, Natural convection in porous triangular enclosures with a solid adiabatic fin attached to the horizontal wall, Int. Commun. Heat Mass Transfer 34 (1) (2007) 19–27.
[25] A. Koca, H.F. Oztop, Y. Varol, The effects of Prandtl number on natural convection in triangular enclosures with localized heating from below, Int. Commun. Heat Mass Transfer 34 (4) (2007) 511–519.
[26] T. Basak, S. Roy, C. Thirumalesha, Finite element analysis of natural convection in a triangular enclosure: effects of various thermal boundary conditions, Chem. Eng. Sci. 34 (4) (2007) 511–519.
[27] S. Kimura, A. Bejan, The heatline visualization of convective heat-transfer, J. Heat Transfer Trans. ASME 105 (4) (1983) 916–919.
[28] A. Bejan, Convection Heat Transfer, third ed., Wiley, Hoboken, NJU, 1984.
[29] F.L. Bello-Ochende, A heat function formulation for thermal convection in a square cavity, Int. Commun. Heat Mass Transfer 15 (1988) 193–202.
[30] V.A.F. Costa, Unification of the streamline, heatline and massline methods for the visualization of two-dimensional transport phenomena, Int. J. Heat Mass Transfer 42 (1) (1999) 27–33.

[31] V.A.F. Costa, Heatline and massline visualization of laminar natural convection boundary layers near a vertical wall, Int. J. Heat Mass Transfer 43 (20) (2000) 3765–3774.
[32] V.A.F. Costa, Unified streamline, heatline and massline methods for the visualization of two-dimensional heat and mass transfer in anisotropic media, Int. J. Heat Mass Transfer 46 (8) (2003) 1309–1320.
[33] V.A.F. Costa, Bejan's heatlines and masslines for convection visualization and analysis, Appl. Mech. Rev. 59 (3) (2006) 126–145.
[34] A. Mukhopadhyay, X. Qin, S.K. Aggarwal, I.K. Puri, On extension of heatline and massline concepts to reacting flows through use of conserved scalars, J. Heat Transfer Trans. ASME 124 (4) (2002) 791–799.
[35] A. Mukhopadhyay, X. Qin, S.K. Aggarwal, I.K. Puri, Visualization of scalar transport in non-reacting and reacting jets through a unified "heatline" and "massline" formulation, Numer. Heat Transfer A 44 (7) (2003) 683–704.
[36] Q.H. Deng, G.F. Tang, Numerical visualization of mass and heat transport for conjugate natural convection/heat conduction by streamline and heatline, Int. J. Heat Mass Transfer 45 (11) (2002) 2373–2385.
[37] A. Dalal, M.K. Das, Heatline method for the visualization of natural convection in a complicated cavity, Int. J. Heat Mass Transfer 51 (1–2) (2008) 263–272.
[38] J.N. Reddy, An Introduction to the Finite Element Method, McGraw-Hill, New York, 1993.
[39] S. Roy, T. Basak, Finite element analysis of natural convection flows in a square cavity with non-uniformly heated wall(s), Int. J. Eng. Sci. 43 (8–9) (2005) 668–680.
[40] V. Erenburg, A.Y. Gelfgat, E. Kit, P.Z. Bar-Yoseph, A. Solan, Multiple states stability and bifurcations of natural convection in a rectangular cavity with partially heated vertical walls, J. Fluid Mech. 492 (2003) 63–89.